Comparative Study on Wear and Corrosion Behavior of Plasma Sprayed $Fe_{73}Cr_2Si_{11}B_{11}C_3$ and $Fe_{63}Cr_9P_5B_{16}C_7$ Metallic Glass Composite Coatings

Anil Kumar[1] · Sapan K. Nayak[1] · Tapas Laha[1]

Abstract In the present study, Fe-based metallic glass composite coatings were synthesized by using two different low-Cr and inexpensive alloying elements containing compositions of $Fe_{73}Cr_2Si_{11}B_{11}C_3$, at. % (P1) and $Fe_{63-}Cr_9P_5B_{16}C_7$, at. % (P2) to investigate their wear and corrosion properties. The coatings were synthesized under optimum spraying parameters via atmospheric plasma spraying (APS), and microstructural characterization showed that the coatings were dense (porosity < 5%) and primarily consisted of amorphous phase (amorphicity level > 84%). Interestingly, corrosion resistance of the P1 powder-based coating was comparable to high-Cr containing plasma-sprayed stainless steel (SS316L) coating despite very low Cr content, which is ascribed to the higher level of amorphicity. The P2-based coating exhibited superior corrosion resistance, attributed to a better combination of lower porosity ($\sim 3.3\%$), the presence of amorphous phase and formation of higher amount of protective α-CrOOH and $Fe_{2-x}Cr_xO_3$. Both the coatings exhibited higher wear resistance compared to the stainless steel coating. Nonetheless, P2-based coating displayed better anti-wear behavior, which was ascribed to its denser microstructure and presence of relatively higher content of hard Fe-based intermetallics. P2-based coating displayed higher value of wear property parameter (H/E_r, 0.073), lower specific wear rate (6.1×10^{-6} mm^3/Nm) and lower coefficient of friction (0.13), signifying excellent wear resistance.

✉ Anil Kumar
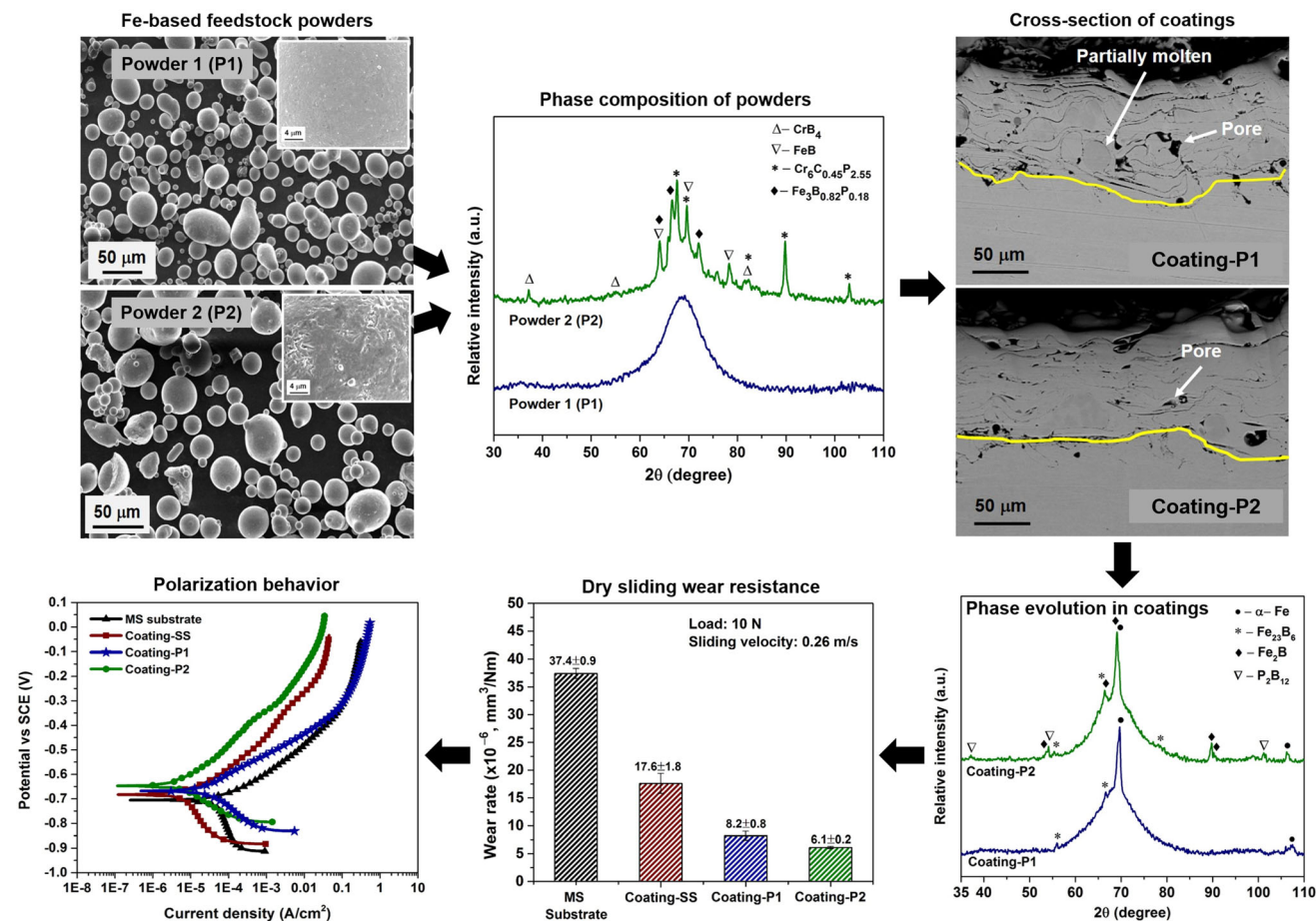   kumar.anilsah14@gmail.com

✉ Tapas Laha
   laha@metal.iitkgp.ac.in

[1] Department of Metallurgical and Materials Engineering, Indian Institute of Technology Kharagpur, Kharagpur, WB 721302, India

Graphical Abstract

Introduction

Iron (Fe)-based metallic glass coatings exhibit the characteristics such as outstanding corrosion resistance, excellent wear resistance, ultra-high hardness and low material cost (Ref 1-4). These extraordinary combinations of properties of such coatings have drawn extensive attention as promising alternative to protect large or expensive structural components in aggressive environments (Ref 5-10). Unfortunately, lack of plasticity at room temperature is the main drawback of such single phase amorphous coatings, which limits their practical engineering applications. Therefore, developing an in situ composite, i.e., amorphous/ nanocrystalline microstructure (amorphous matrix embedded with secondary crystalline phases) is considered to be very useful to circumvent the inherent brittleness of these coatings (Ref 8-11). Such amorphous/ nanocrystalline composite structure display remarkably enhanced plasticity and considerably improved hardness, impact toughness and wear resistance (Ref 8, 12-15). However, formation of secondary crystalline phases in the amorphous matrix leads to localized compositional variation which can impair the corrosion resistance of the coatings in saline environments (Ref 8, 16-21).

Besides, the choice of chemical composition also plays an important role in controlling the wear and corrosion resistance of Fe-based amorphous alloys. Their wear and corrosion resistance can be significantly improved with the addition of alloying elements like Mo, Co, Ni, Y, Zr, Cr, W, etc. (Ref 1, 22-25). However, these elements are expensive which limits the widespread applications of these alloys. From corrosion perspective, Cr is considered as the most important alloying element because it forms a Cr-based stable passive film that inhibits the dissolution of amorphous matrix (Ref 1, 2, 16). Addition of P and Si to Fe-Cr-based alloys further improves their corrosion resistance (Ref 1, 22, 23, 25). In terms of wear behavior, use of

B and C as alloying elements can promote the formation of Fe-borides and Fe-carbides which are beneficial for improving the hardness and wear resistance (Ref 3, 18, 22, 25, 26). Not to mention, addition of these inexpensive metalloids (e.g., C, P, B and Si) significantly improves the glass-forming ability (GFA) of Fe-based systems (Ref 25, 27). Therefore, synthesis of a Fe-Cr-based amorphous alloy with low-cost metalloids without adding expensive elements is of great significance for wear and corrosion resistance applications. Especially, with an appropriate composition, synthesis of Fe-Cr-based amorphous composite coatings has gained greater research interest as protective coatings to be used in harsh conditions (Ref 2, 3, 9). In recent years, several efforts have been made for the synthesis of Fe-based glassy composite coatings by thermal spraying processes such as atmospheric plasma spray (APS), high-velocity oxygen/air-fuel spray (HVOF/HVAF), arc spray and cold spray (Ref 2, 3, 8-12, 28). Among these techniques, APS have a slightly upper hand in terms of synthesizing metallic glass composite coatings because of the high deposition rate, flexibility and low cost. APS provides ultra-high cooling rate of around 10^5-10^7 K/s, which inhibits long-range atomic diffusion and leads to formation/retention of amorphous phase.

In this study, low Cr and inexpensive alloying elements containing two different feedstock powders were used to synthesize plasma sprayed Fe-based metallic glass composite coatings. Comprehensive investigation was carried out to understand the phase formation and microstructural features of the coating and their subsequent effect on wear and corrosion resistance properties. Besides, different length scale wear study was carried out to evaluate the influence of porosity as well as constituent phases in the coating. Post-corrosion Raman analysis was carried out to estimate a relative protective index parameter (α^*/γ^* ratio) for establishing a relationship between the corrosion resistance and the constituent phases of corrosion products. The properties of the glassy coatings were also compared with plasma-sprayed stainless steel (SS316L) coating and mild steel substrate to understand the relative protection ability.

Experimental Procedure

Synthesis of Plasma-sprayed Coatings

Two different low Cr containing feedstock powders with compositions of $Fe_{73}Cr_2Si_{11}B_{11}C_3$, at. % (P1) and $Fe_{63}Cr_9P_5B_{16}C_7$, at. % (P2) were used to synthesize Fe-based metallic glass composite coatings. These chosen alloy compositions possess high potential for industrial applications because of their high GFA and relatively low cost of the alloying elements. The feedstock powders P1 and P2 were synthesized by gas and water atomization, respectively. A detailed explanation on higher GFA of the feedstock powders has been provided in Section ''Glass-Forming Ability Based on Thermodynamic Parameter P_{HSS}''. As getting amorphous structure in P1 was difficult via water atomization process, ascribed to its relatively lower GFA (P_{HSS} = −3.1 kJ/mol), therefore this powder was produced by gas atomization process where fully amorphous structure was obtained. In the case of gas atomization, atomization chamber is kept vacuum-tight which enables the formation of oxidation free fully amorphous spherical powders. However, this process is complex and costly. On the other hand, amorphous structure was obtained in P2 via simpler and economical water atomization process, attributed to the high GFA (P_{HSS} = −7.3 kJ/mol).

Commercially available $Fe_{73}Cr_2Si_{11}B_{11}C_3$, at. % (P1) amorphous powder prepared by inert gas atomization was procured from Epson Atmix Corporation, Japan. While powder P2 was synthesized via water atomization using industrial grade raw materials. Water atomization was carried out with atomization pressure of 160 bar, metal flow rate of 25 to 30 kg·min^{-1}, water flow rate of 280 L·min^{-1} while maintaining inert (Ar) atmosphere in the atomization chamber. Boron, chromium and phosphorus were incorporated in the master alloy as ferro-boron, ferro-chrome and ferro-P, respectively, as per the composition. Cold rolled scrap of Fe was the primary source of Fe.

Coatings were deposited onto grit-blasted mild steel substrates by atmospheric plasma spraying process under optimum spraying parameters using a commercial Plasma F-4 (Metallizing Equipment Company Pvt. Ltd., India) plasma spray torch. To synthesize the P1- and P2-based coatings with minimum porosity and maximum achievable amorphous content, proper powder feed rate was determined initially, and then gas flow rate, standoff distance and other parameters were optimized. Forced air cooling was continuously applied to the coatings and steel substrates to avoid the heat accumulation effect during the deposition of the coatings and to maximize the amorphous phase formation. The details of optimized spraying parameters are listed in Table 1. Besides, stainless steel (SS316L) coating was synthesized using optimized industrial parameters to compare the Fe-based amorphous composite coatings with stainless steel coating. Coatings deposited with P1, P2 and water-atomized SS316L powders are represented as Coating-P1, Coating-P2 and Coating-SS, respectively.

Table 1 Plasma spray parameters used to synthesize the Fe-based metallic glass composite coatings

Coatings	Plasma power (kW)	Powder feed rate (g/min)	Primary gas (Ar) flow rate (L/min)	Secondary gas (H$_2$) flow rate (L/min)	Spray distance (mm)	Coating thickness (μm)
Coating-P1	30	40	60	10	120	120 ± 15
Coating-P2						

Microstructural and Morphological Study

The structure and morphology of the feedstock powders and coatings were analyzed by scanning electron microscopy (SEM, SUPRA 40, Carl Zeiss AG, Germany). The average porosity level in the coatings was evaluated by image processing, which was done on 15 cross-sectional SEM micrographs (obtained from different regions of the coatings at a magnification of 500 x) using ImageJ k 1.45 software. The phase constitutions of the atomized powders and the coatings were detected by x-ray diffraction (PANalytical-Empyrean, Netherlands, DY1705; Cr-Kα radiation). The crystalline and amorphous nature of the coatings was further investigated using transmission electron microscopy (FEG-TEM, JEOL, JEM-2100F). Thermal stability of the feedstock powders and coatings was analyzed by using a differential scanning calorimeter (DSC, NETZSCH STA 449 F3) at a heating rate of 10 K/min under Ar atmosphere.

Indentation and Wear Test

In consideration of the microstructural inhomogeneity in the coatings, microhardness was evaluated from 15 measurements conducted at a load of 25 gf using a Vickers micro indenter (UHLVMHT-001, Walter Uhl, Germany). Nanoindentation tests were carried out using a Triboindenter (TI 950, Hysitron Inc., USA) with Berkovich tip (TI-0039, Hysitron Inc., total included an angle of 142.3° and tip radius of 100 nm) to measure nanohardness (H) and reduced modulus (E$_r$) at different regions of the top surface of the coatings. A maximum load of 5000 μN with a loading rate of 500 μN/s and a peak load hold time of 10 s was applied. The average values of nanohardness and modulus were obtained from 100 indents (10 × 10 matrix of indents). Constant loading (load of 5000 μN) nano-scratch tests were carried out using a Hysitron Triboindenter (TI 950, USA) with Berkovich tip (TI-0039, total included an angle of 142.3° and tip radius of 100 nm) with a traverse speed of 0.5 μm/s to obtain a scratch length of 10 μm. The scratch tracks were investigated by in situ scanning probe microscopy (SPM) to observe their morphology and calculate nanowear volume. Dry sliding wear tests were carried out with a pin-on-disk tribometer (TE97 Friction and Wear Demonstrator, Phoenix Tribology Ltd., England). Sample grounded by using 2000 mesh SiC papers and ultrasonically cleaned in acetone was used as a pin, and held against a rotating counterpart material Al$_2$O$_3$ disk. After polishing, roughness of the pin and Al$_2$O$_3$ disk were measured by using Veeco DEKTAK 150 profilometer and the value of average surface roughness (R$_a$) was found to be 1.35 ± 0.11 μm, 1.21 ± 0.07 μm, 1.18 ± 0.06 μm, 0.42 ± 0.03 μm and 0.11 ± 0.01 μm for Coating-P1, Coating-P2, Coating-SS, substrate and Al$_2$O$_3$ disk, respectively. The parameters used for wear test are as follows: applied load of 10 N, rotating speed of 0.26 m/s, wear track radius of 25 mm and a fixed total sliding distance of 235 m. At least three sliding tests were conducted for each sample from the repeatability perspective. The wear resistance of the samples was compared in terms of wear rate which was calculated using an equation (Ref [29], [30]), $Q = \frac{V_w}{NS}$, where Q is wear rate in mm^3/Nm, V$_w$ is wear volume (mm^3), N and S represent applied load (N) and total sliding distance (m), respectively.

Potentiodynamic Polarization Tests

Corrosion resistance of the as-sprayed coatings was evaluated by conducting potentiodynamic polarization tests in aqueous solution of 3.5 wt. % NaCl, using a potentiostat (Interface 1000, Gamry Instruments, USA). Graphite rod and saturated calomel electrode (SCE) were used as the counter and reference electrodes, respectively. Exposed surface area of about 1 cm^2 was used for testing. When open circuit potential (OCP) became stable after the immersion of samples in electrolyte for 1 h, then potentiodynamic polarization test was performed from −0.25 to +0.6 V with respect to OCP at a sweep rate of 0.5 mV/s. From good reproducibility point of view, the tests were repeated three times for each sample. After polarization tests, samples were inspected under SEM to observe the morphology of the corroded samples. Further, Raman spectroscopic analysis was carried out using Renishaw InVia Raman Microscope (UK, Co laser with wavelength of 532 nm) system for identifying the phase composition of

corrosion products which formed on the surface of the coatings during exposure in NaCl solution.

Results and Discussion

Glass-Forming Ability Based on Thermodynamic Parameter P_{HSS}

Several approaches have been proposed by researchers to envisage the glass-forming ability (GFA) of amorphous alloys (Ref 25, 27, 31). Among those thermodynamic parameters, P_{HSS} proposed by Rao et al. is considered to be very effective for predicting the GFA of Fe-based multi-component systems (Ref 32). This parameter includes combined aspects of the thermodynamic and topological approach, and the parameter is expressed as (Ref 32):

$$P_{HSS} = \Delta H_{mix}(\Delta S_{mix}/R)(\Delta S_\sigma/k_B) \qquad \text{(Eq 1)}$$

where ΔH_{mix} is the enthalpy of mixing, ΔS_{mix} is the configurational entropy, R is the gas constant, ΔS_σ is the mismatch entropy and k_B is the Boltzmann's constant. The calculated values of P_{HSS} for $Fe_{73}Cr_2Si_{11}B_{11}C_3$ (at. %, P1) and $Fe_{63}Cr_9P_5B_{16}C_7$ (at. %, P2) were −3.2 and −7.3 kJ/mol, respectively. The values of P_{HSS} parameter of both the compositions lie well within the required range (−11 kJ/mol to −3 kJ/mol) for glass formation which has been established by the experimental results supported with computational methods as reported previously (Ref 31, 32). The GFA of the alloy systems tends to increase with the decreasing values of P_{HSS} within the defined range (Ref 31). The P_{HSS} value of P2 is more negative than that of P1, therefore it can be said that the GFA of P2 is higher compared to P2.

Morphology and Phase Composition of the Powders

Morphology, size distribution and chemical composition of the feedstock powders are presented in Fig. 1. The SEM micrographs as shown in Fig. 1(a) and (b) show that both gas-atomized (P1) and water-atomized (P2) powders are mostly spherical or nearly spherical. The sphericity of the powders resulted from optimization of the atomization processing parameters. High magnification SEM micrographs presented in insets display that the top surface of P1 is smooth while that is relatively rough in the case of P2, which are typical features of gas and water-atomized powders, respectively. The bar charts as presented in Fig. 1(c) and (d) demonstrate that particle size of P1 and P2 varies in the range of 5-60 μm ($D_{mean} \sim 25$ μm) and 5-45 μm ($D_{mean} \sim 18$ μm), respectively. Energy dispersive spectroscopy (EDS) analysis of powders confirms the presence of constituent elements, viz., Fe, Si, Cr and C in P1, while elements such as Fe, Cr, P, C and O were identified for P2, and EDS spectra are shown in Fig. 1(e) and (f). Boron, being of lower atomic weight could not be detected by EDS. From the XRD patterns shown in Fig. 2, it can be observed that P1 exhibited a broad hump, which indicates the formation of a fully amorphous structure during gas atomization. On the other hand, even though the GFA of P2 is higher (as discussed in section. ''Glass-Forming Ability Based on Thermodynamic Parameter P_{HSS}''), XRD pattern of P2 exhibited a broad hump along with several superimposed crystalline peaks. This indicates that crystalline phases in P2 formed during the water atomization process. The presence of 6.8 at. % of oxygen (O) was identified from the EDS spectrum of the outer surface of P2 (Fig. 1f), which would have resulted from the oxidation of powder particles during water atomization. Such level of oxygen content in P2 can lead to formation of oxides that could act as heterogeneous nucleation sites and promt crystalline phase evolution during solidification.

Morphology and Phase Composition of the Coatings

Top surface and cross-sectional morphologies of the as-sprayed coatings are shown in Fig. 3(a, b) and Fig. 3(c, d), respectively. The as-sprayed surfaces as shown in Fig. 3(a) and (b), show that Coating-P1 contains relatively higher extent of partially molten particles compared to Coating-P2, attributed to the larger particle size of P1. Thickness built-up of 120 ± 15 μm is evident from the cross-sectional SEM micrographs presented in Fig. 3(c) and (d). Pore volume fraction estimated by doing quantitative image analysis of the cross-sectional SEM images indicated that the porosity content is less in the coatings. The porosity content was found to be approximately 4.9 ± 0.8 % and 3.3 ± 0.7 % for Coating-P1 and Coating-P2, respectively. The slightly higher porosity content in Coating-P1 could be ascribed to probable insufficient melting of the comparatively larger powder particles of P1 (as shown in Fig. 3c), which caused formation of poorly adhered splats and resulted in inter-lamellar pores.

Figure 4 demonstrates XRD patterns of the P1- and P2-based coatings, which show broad halo peaks overlapped with some crystalline diffraction peaks. The presence of the minor crystalline peaks indicates the formation of composite structure, i.e., crystalline phases embedded in an amorphous matrix. Only two types of phase constituents were identified in Coating-P1 namely α-Fe and $Fe_{23}B_6$, while more crystalline phases were identified in the case of Coating-P2, viz., α-Fe, Fe_2B, $Fe_{23}B_6$ and P_2B_{12}. Amorphicity level of Coating-P1 and Coating-P2 estimated from the area ratio of crystalline peaks to amorphous hump was
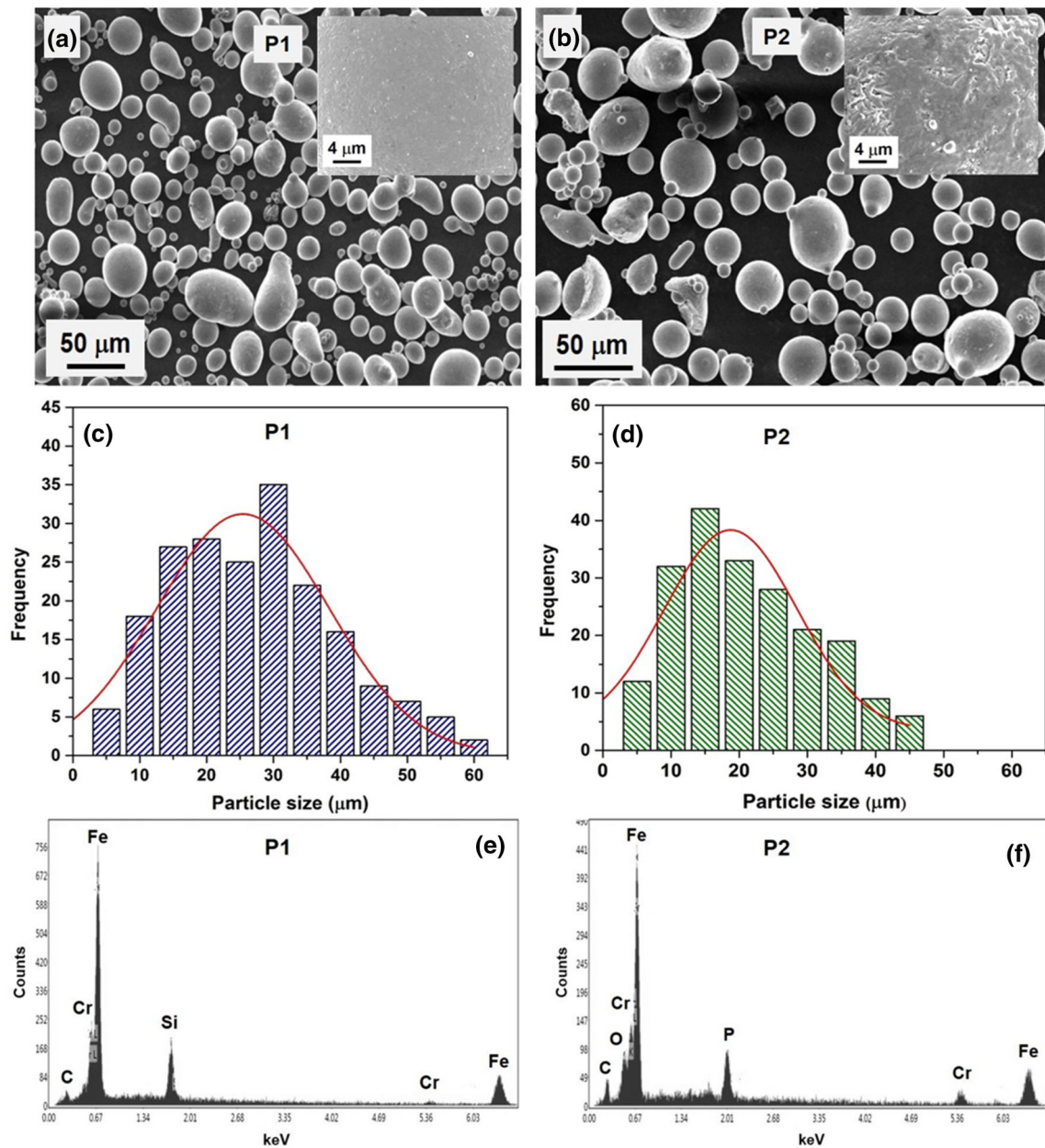
Fig. 1 Morphology, size distribution and chemical composition of P1 and P2 powders: (a, b) SEM micrographs and their corresponding high magnification micrographs (in insets), (c, d) powder particle size distribution and (e, f) EDS spectrum obtained from the outer surface of powder particles

approximately 87.8 % and 84.2 %, respectively. Formation of the crystalline phase in the coatings can be ascribed to the heat input, heat accumulation and partial oxidation of powder particles during the coating deposition (Ref 12, 16, 20, 30). The relatively lower amorphous content in Coating-P2, even though P2 possesses higher GFA, can be attributed to the pre-existing crystalline phases in P2, which would have been retained due to the incomplete melting of some of the powder particles. Also, the presence of crystalline phases in amorphous matrix acts as heterogeneous nucleation sites and therefore leads to higher

degree of devitrification during solidification from the liquid state. TEM micrographs of the coatings as shown in Fig. 5(a) and (b) confirm the existence of nano-sized crystalline phases distributed in the amorphous matrix, and this observation matches well with the corresponding SAED patterns (Fig. 5c, d). The spotted rings in SAED pattern indicate the crystalline phases and diffused background confirms the presence of amorphous matrix in the coatings. Besides, higher grain number density and formation of larger grains in Coating-P2 indicate that amorphous content in this coating is lower compared to Coating-

P1 (also evident from XRD analysis as discussed earlier, Fig. 4).

Figure 6 shows DSC thermograms of P1 and P2 powders and metallic glass composite coatings. Feedstock powder and coating of the same composition exhibit exothermic peaks located nearly at the same position. P1-based powder and coating experience onset of crystallization around 538 °C, while P2-based powder and coating showed onset of crystallization around 573 °C. Crystallization enthalpy value associated with the exothermic peak has been determined to be −61 kJ and −21 kJ for P1- and P2-based powders while −45 kJ and −38 kJ for P1- and P2-based coatings, respectively. Higher value of enthalpy for crystallization is indicative of higher degree of amorphicity, therefore, it can be said that amorphous content in P1-based powder and coating is higher compared to P2-based powder and coating. This finding is also consistent with XRD and TEM analyses.
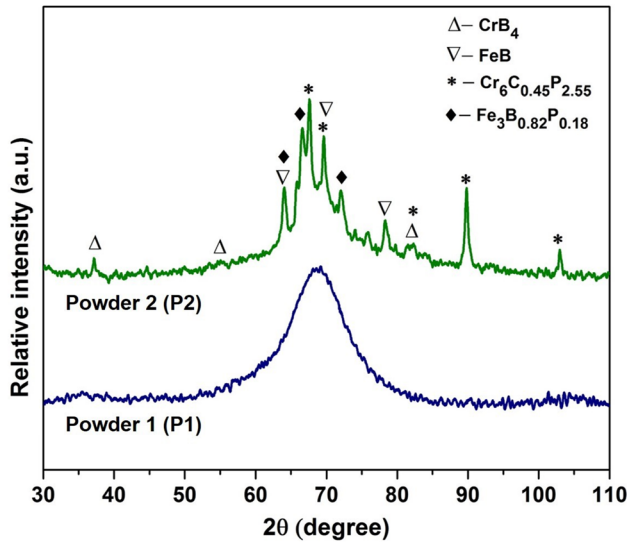

Fig. 2 XRD patterns of P1 and P2 powders displaying fully amorphous and amorphous/ crystalline structure, respectively

Fig. 4 XRD patterns of the as-sprayed P1- and P2-based coatings, exhibiting variation in the extent of crystallization

Fig. 3 SEM micrographs of (a, b) as-sprayed surface and (c, d) cross-sectional morphologies of P1 and P2-based plasma-sprayed coatings

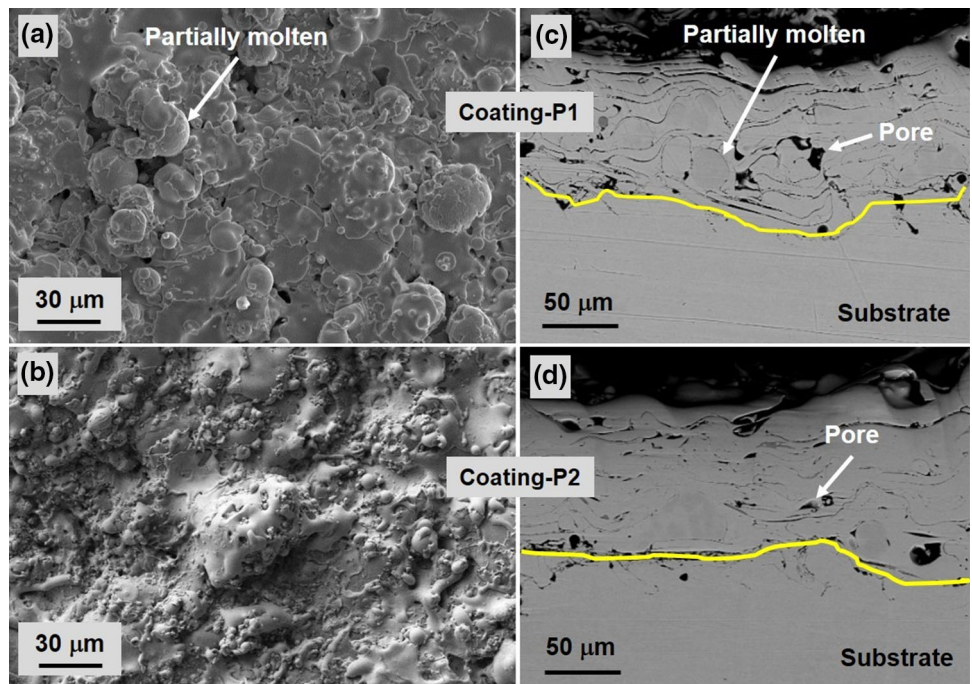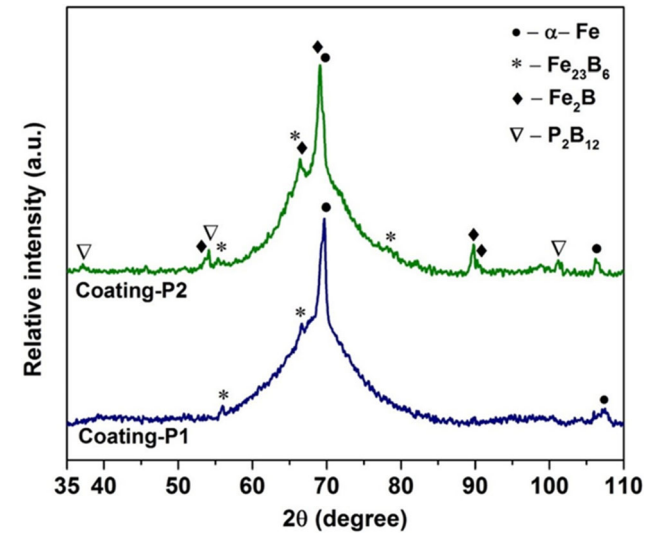**Fig. 5** (a, b) Bright field TEM micrographs and (c, d) corresponding SAED patterns of P1- and P2-based metallic glass composite coatings

and mild steel substrate obtained from microindentation and nanoindentation tests are reported in Table 2. Average Vickers microhardness of Coating-P1, Coating-P2, Coating-SS and mild steel was 942 ± 70, 1019 ± 53, 560 ± 46 and 172 ± 10 $HV_{0.025}$, respectively, and average nanohardness was approximately 9.8 ± 2.2, 10.5 ± 2.0, 6.7 ± 3.2 and 3.6 ± 0.2, respectively. The ultra-high hardness values were obtained in case of Coating-P1 and Coating-P2 compared to Coating-SS and mild steel substrate, which is attributed to the presence of composite structure (amorphous matrix embedded with nanocrystalline phases) in the glassy coatings. Besides, relatively higher hardness of Coating-P2 than that of Coating-P1 can be attributed to (i) denser microstructure and (ii) higher content of hard intermetallic phases (as evident from XRD analysis reported in Section ''Morphology and Phase Composition of the Coatings'').

The average reduced elastic modulus (E_r) obtained from nanoindentation for Coating-P1, Coating-P2, Coating-SS and mild steel were 139 ± 31 and 143 ± 34, 168 ± 22 and 185 ± 6 GPa. Both Coating-P1 and Coating-P2 have lower average elastic modulus than that of Coating-SS and mild steel, which is because of the highly amorphous structure of the P1- and P2-based coatings. Due to the presence of
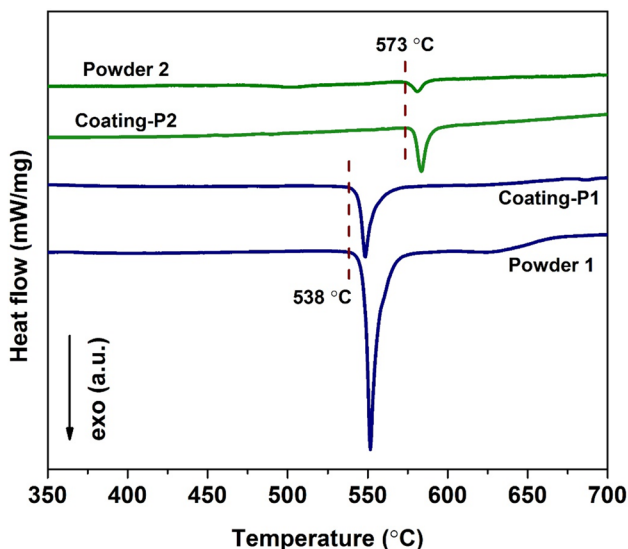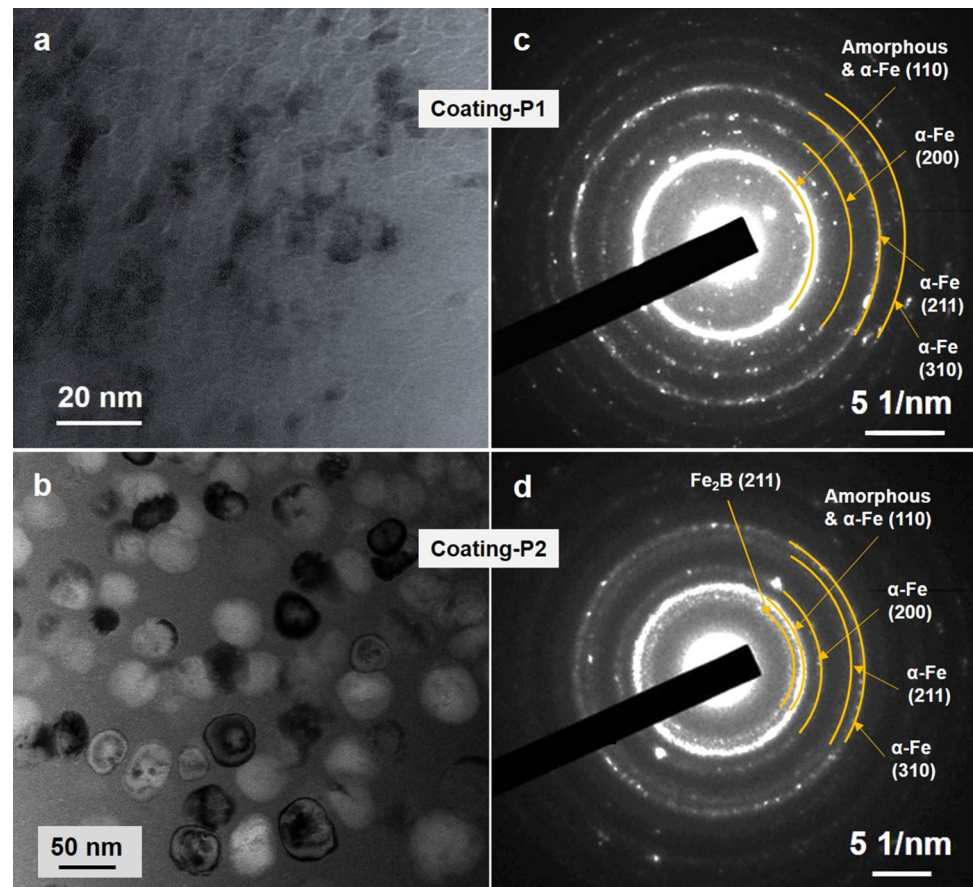

Fig. 6 DSC thermograms of P1- and P2-based powders and metallic glass composite coatings

Mechanical Properties of the Coatings

Values of the various mechanical properties of the Fe-based metallic glass composite coatings, SS316L coating

Table 2 Porosity, amorphous content and various mechanical properties obtained for the glassy composite coatings, stainless steel (SS316L) coating and mild steel substrate

Samples	Coating-P1	Coating-P2	Coating-SS	MS substrate
Porosity (vol. %)	4.9 ± 0.8	3.3 ± 0.7	2.5 ± 0.3	…
Amorphous content (%)	87.8	84.2	…	…
Vickers microhardness ($HV_{0.025}$)	942 ± 70	1019 ± 53	560 ± 46	172 ± 10
Nanohardness (H, GPa)	9.8 ± 2.2	10.5 ± 2.0	6.7 ± 3.2	3.6 ± 0.2
Reduced elastic modulus (E_r, GPa)	139 ± 31	143 ± 34	168 ± 22	185 ± 6
Wear property parameter, H/E_r	0.070	0.073	0.039	0.019
Nanowear volume per unit length ($\times 10^{-9}$ mm^3/mm)	0.71	0.53	1.22	3.45
Coefficient of friction (Dry Sliding wear)	0.18 ± 0.03	0.13 ± 0.02	0.28 ± 0.04	0.47 ± 0.06

free volume in amorphous alloys, the inter-atomic distance is found to be more in these materials compared to crystalline alloys. Large inter-atomic distance weakens the atomic bonding and therefore reduces the elastic modulus in amorphous alloys. Relatively higher value of modulus in Coating-P2 compared to Coating-P1 can be ascribed to (i) lower porosity content (Table 2) and (ii) higher degree of crystallization (Fig. 4 and 5) in Coating-P2. Free volume of amorphous alloys starts annihilating after crystallization, consequently, a relaxed structure with shorter inter-atomic distance develops, which leads to higher modulus. On the other hand, despite of Coating-SS having crystalline structure, showed lower modulus compared to mild steel substrate, attributed to the presence of porosity in this coating.

The nanoindentation data (i.e., H and E_r) were used to calculate the wear resistance parameter (i.e., ratio of H/E_r) of the various samples. The values of H/E_r ratio for Coating-P1, Coating-P2, Coating-SS and mild steel 0.070, 0.073, 0.039 and 0.019, respectively (also listed in Table 2). Leyland et al. observed that materials having a higher value of H/E_r ratio exhibit higher wear resistance (Ref 33). According to findings reported by Mukhopadhyay et al. (Ref 34), materials can display higher extent of elastic recovery if their H/E_r ratio value is greater than 0.05 which is considered as a very useful parameter for defining higher wear resistance. This finding suggests that Coating-P2 should display better wear resistance compared to the other coatings (P1 and SS).

## Multi-scale Wear Behavior of the Coatings

Investigation of Nanoscale Wear by Nanoscratch Test

The wear behavior of plasma sprayed coatings gets significantly affected by microstructural heterogeneities such as multilayered splats, inter-splat bonding and associated porosity (Ref 12-16). The deformation behavior of individual splats of such coatings can only be studied by lower length scale test with lower level of loading. Therefore, low load nanoscratch tests (load of 5000 μN and scratch length of 10 μm) were carried out to understand the single splat wear behavior of the plasma-sprayed metallic glass composite coatings. In this method, the wear resistance of the P1- and P2-based coatings was evaluated from scratch groove profiles (i.e., scratch width and depth) and wear volume. SPM images of scratch tracks and their cross-sectional depth profiles resulting from the nanoscratch test are presented in Fig. 7. The SPM images reveal that there are significant differences in the scratch width and depth of the various coatings, insinuating different response against wear of these coatings. When Berkovich tip is used for nanoscratch test, then wear volume (W_V) per unit length, which is directly related to the wear rate, can be calculated by using Eq 2 (Ref 35).

$$W_v = \frac{1}{2}\cos(70.3°) \cdot d_n^2 \tag{Eq 2}$$

where, d_n represents normal displacement. The values of wear volume acquired from the nanoscratch tests for Coating-P1, Coating-P2, Coating-SS and mild steel were 0.71×10^{-9}, 0.53×10^{-9}, 1.22×10^{-9} and 3.45×10^{-9} mm^3/mm, respectively (also listed in Table 2). Higher wear volume is indicative of poor wear resistance, therefore, it can be said that Coating-P2 possessed the superior wear resistance (also evident from the calculated

Fig. 7 In-situ SPM images of nanoscratch tracks made on (a, b) P1- and P2-based coatings, (c) stainless steel (SS316L) coating and (d) mild steel substrate, and (e) 2D cross-sectional scratch depth profiles of these samples
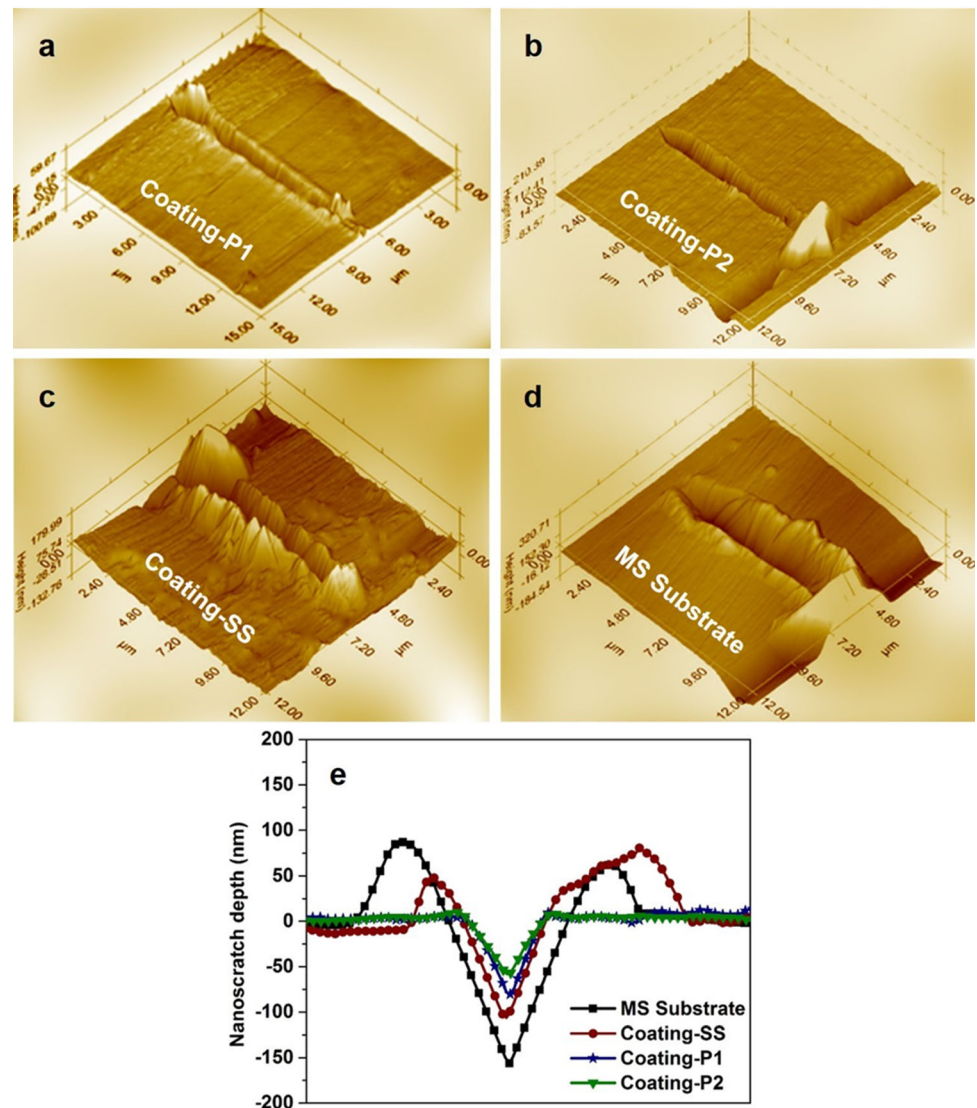
value of H/E$_r$, Table 2), ascribed to the presence of harder intermetallic phases in the amorphous matrix. From the wear rate values as mentioned above, it can be observed that wear resistance of the mild steel can be improved by 2.8 times after applying Coating-SS, while it can be improved by 6.5 times in case of Coating-P2.

Investigation of Macroscale Wear by Dry Sliding Wear Test

Nanoscratch tests, as detailed in the previous section, were carried out to mainly investigate the wear behavior of individual splats for understanding the influence of material properties (H and E$_r$) on the wear resistance of the coatings. To understand the global deformation behavior of the coatings, which includes effect of all the heterogeneities (inter-splat boundaries, porosities, crystalline phases, etc.) present in the coatings, macroscale wear

characterization was done by using pin-on-disk dry sliding wear test. The results obtained from the dry sliding wear tests are shown in Fig. 8. The coefficient of friction (COF) curves as a function of sliding distance are demonstrated in Fig. 8a, and the values of COF are presented in Table 2. Average values of COF for Coating-P1, Coating-P2, Coating-SS and mild steel were found to be 0.18 ± 0.03, 0.13 ± 0.02, 0.28 ± 0.04 and 0.47 ± 0.06, respectively. This shows that metallic glass coatings have better anti-wear properties compared to stainless steel coating. The lowest value of COF was observed in case of Coating-P2, implying that this coating has better anti-wear properties. Specific wear rate values obtained from dry sliding wear tests are presented in Fig. 8b. The specific wear rate of Coating-P1, Coating-P2, Coating-SS and mild steel was 8.2 ± 0.8 × 10^{-6}, 6.1 ± 0.2 × 10^{-6}, 17.6 ± 1.8 × 10^{-6} and 37.4 ± 0.9 × 10^{-6} mm^3/Nm, respectively. Both the
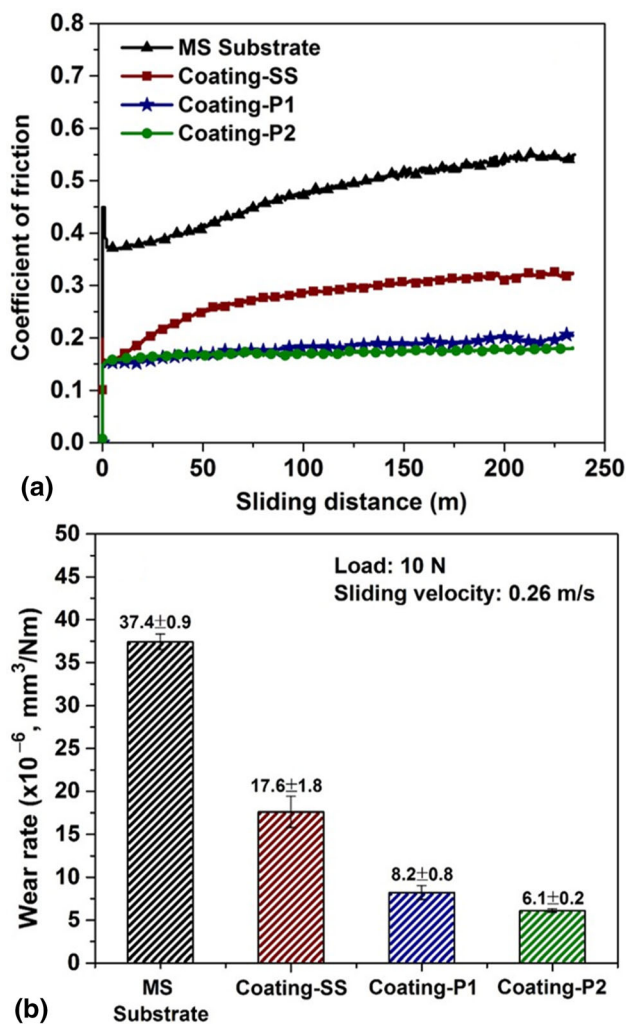
Fig. 8 (a) Coefficient of friction vs. sliding distance curves and (b) bar graph of wear rate values of the glassy composite coatings, stainless steel (SS316L) coating and mild steel obtained from dry sliding wear testing

metallic glass coatings exhibited lower wear rate than that of stainless steel coating and mild steel substrate.

It is also worth mentioning here that wear resistance of Coating-P2 is superior to Coating-P1, ascribed to its ultra-high microhardness (1019 $HV_{0.025}$) that resulted due to the denser microstructure (porosity $\sim$ 3.3 %) and presence of relatively higher content of hard Fe-based intermetallics. Besides, wear behavior of amorphous alloys depends on both hardness and toughness, a good balance between the hardness and toughness increases the wear resistance (Ref 14). A certain amount of nano-sized crystalline phase increases both the hardness and the toughness of amorphous alloys, consequently enhances their wear resistance. The value of specific wear rate of metallic glass composite coatings is typical of Fe-based bulk metallic glass containing nanocrystals (Ref 18, 19). The values of COF and wear rate of the metallic glass coatings and mild steel
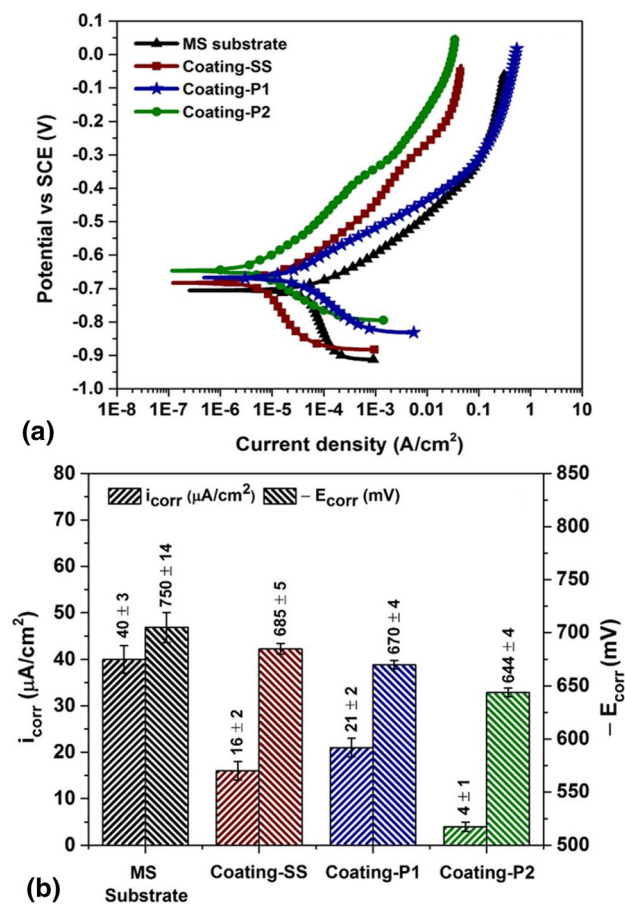

Fig. 9 (a) Potentiodynamic polarization curves and (b) bar graph of corrosion current density (i_{corr}) and corrosion potential (E_{corr}) values of the P1- and P2-based coatings, stainless steel (SS316L) coating and mild steel substrate

substrate used in the present work were found to be in a similar range of the COF and wear rate values of Fe-based amorphous coatings and mild steel reported by Burkov et al. (Ref 36) and Ham et al. (Ref 37) via pin-on-disk wear test.

Electrochemical Behavior

The corrosion properties of the coatings were investigated by conducting potentiodynamic polarization tests in 3.5 wt. % NaCl solution and the results are reported in Fig. 9, 10, 11, 12. Polarization curves acquired from the polarization tests and corresponding corrosion potential (E_{corr}) as well as current density (i_{corr}) values are reported in Fig. 9. Values of E_{corr} for Coating-P1, Coating-P2, Coating-SS and mild steel were -670 ± 4, -644 ± 4, -685 ± 5 and -750 ± 14 mV$_{SCE}$, respectively, and values of i_{corr} were 21 ± 2, 4 ± 1, 16 ± 2 and 40 ± 3 μA/cm^2, respectively. Coating-P2 exhibited superior corrosion resistance in terms of the highest positive E_{corr} and the lowest i_{corr} values.

Fig. 10 Surface morphologies of (a, b) of the glassy composite coatings, (c) stainless steel (SS316L) coating and (d) mild steel after potentiodynamic polarization test in 3.5 wt. % NaCl solution
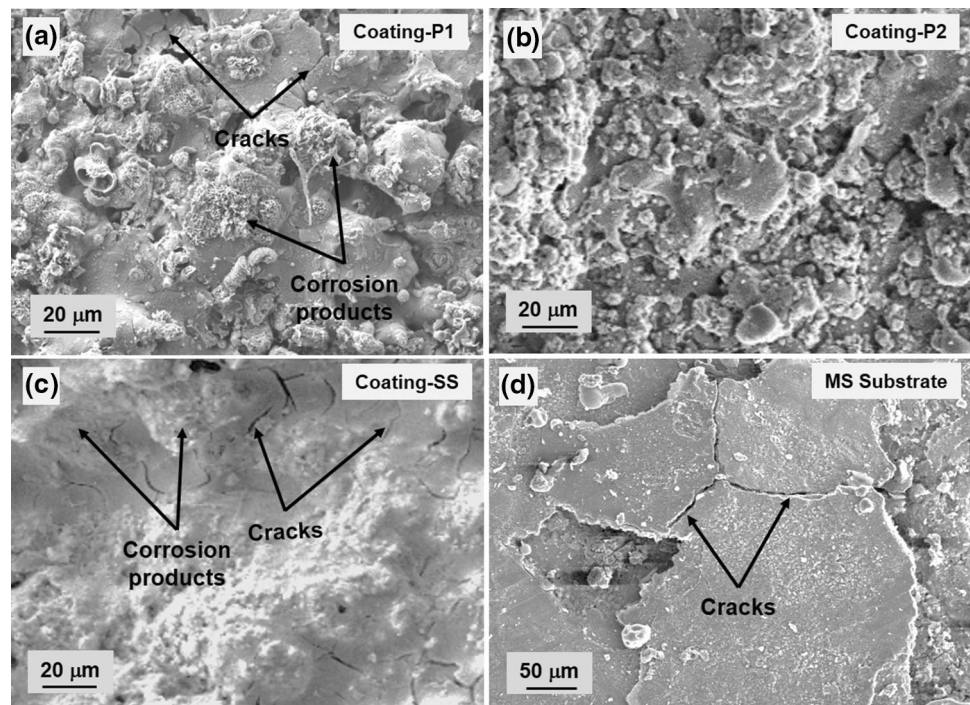
Higher positive potential indicates that Coating-P2 has a superior tendency for stability in NaCl solution, and lower i_{corr} value signifies its superior corrosion resistance. Coating-P2 exhibited very low i_{corr} value (4 $\mu A/cm^2$) despite the absence of expensive elements, viz., Mo, Ni, etc., which are used to improve the corrosion resistance of Fe-based metallic glasses. Interestingly, Coating-P2 shows signature of weak passivation to some degree with a breakdown at around −400 mVSCE in anodic polarization curve, which could be ascribed to the formation of higher fraction of Cr-based protective corrosion products (it has been explained later in this section). The above-mentioned findings indicate that effect of Si addition on corrosion resistance is not very evident because Coating-P1 showed lower E_{corr} and higher i_{corr} values compared to Si-free Coating-P2. Also, passivation tendency in polarization curve was not observed in case of P1-based metallic glass coating. In the previously reported literature, it was found that addition of Si further improves the corrosion resistance of Fe-based metallic glass due to formation of SiO_2 passive film (Ref 1). But, in the present study, it has been observed that effect of other factors, viz., crystallinity, porosity, etc., on corrosion resistance of Coating-P1 is more prominent compared to the presence of Si.

In addition, the corrosion resistance of the present metallic glass coatings (Coating-P1 and Coating-P2) in the saline environment is found to be comparable to the Fe-based amorphous coatings synthesized via plasma spraying by Zhang et al. (Ref 38) and Jiang et al. (Ref 39). In these plasma-sprayed coatings high-cost alloying elements, viz.,

Cr, Mo and Ni were used to improve their corrosion properties. The value of corrosion potential was −578.84 mV and −750 mV, and the value of corrosion current density was 1.887 $\mu A/cm^2$ and 150 $\mu A/cm^2$ for the coatings deposited by Zhang et al. and Jiang et al, respectively. These observations indicate that the metallic glass coatings, i.e., Coating-P1 (E_{corr}: −670 mV, i_{corr}: 21 $\mu A/cm^2$) and Coating-P2 (E_{corr}: −644 mV, i_{corr}: 4 $\mu A/cm^2$) synthesized in the present work have high corrosion resistance despite low Cr content and the absence of costly elements like Mo and Ni.

SEM micrographs of post-corroded samples (after exposure in NaCl solution) revealed that surfaces of the metallic glass coatings (Fig. 10a, b) were of different morphological features. In the case of Coating-P1, larger portion of the coating's surface was non-uniformly covered with corrosion products along with smaller cracks (Fig. 10a). Coating-P2 showed almost no visible cracks (Fig. 10b), elucidating its excellent corrosion resistance. Small cracks were also revealed on the surface of Coating-SS (Fig. 10c), indicating comparatively poor corrosion resistance. On the other hand, mild steel (Fig. 10d) displayed severe cracking, demonstrating very low corrosion resistance. To further understand the corrosion process involved during the potentiodynamic polarization test, corrosion products formed on the surface of the samples have been identified via Raman spectroscopy and the acquired Raman spectra are presented in Fig. 11. Each single deconvoluted peak represents the individual Lorentzian fit associated with a particular phase present in the
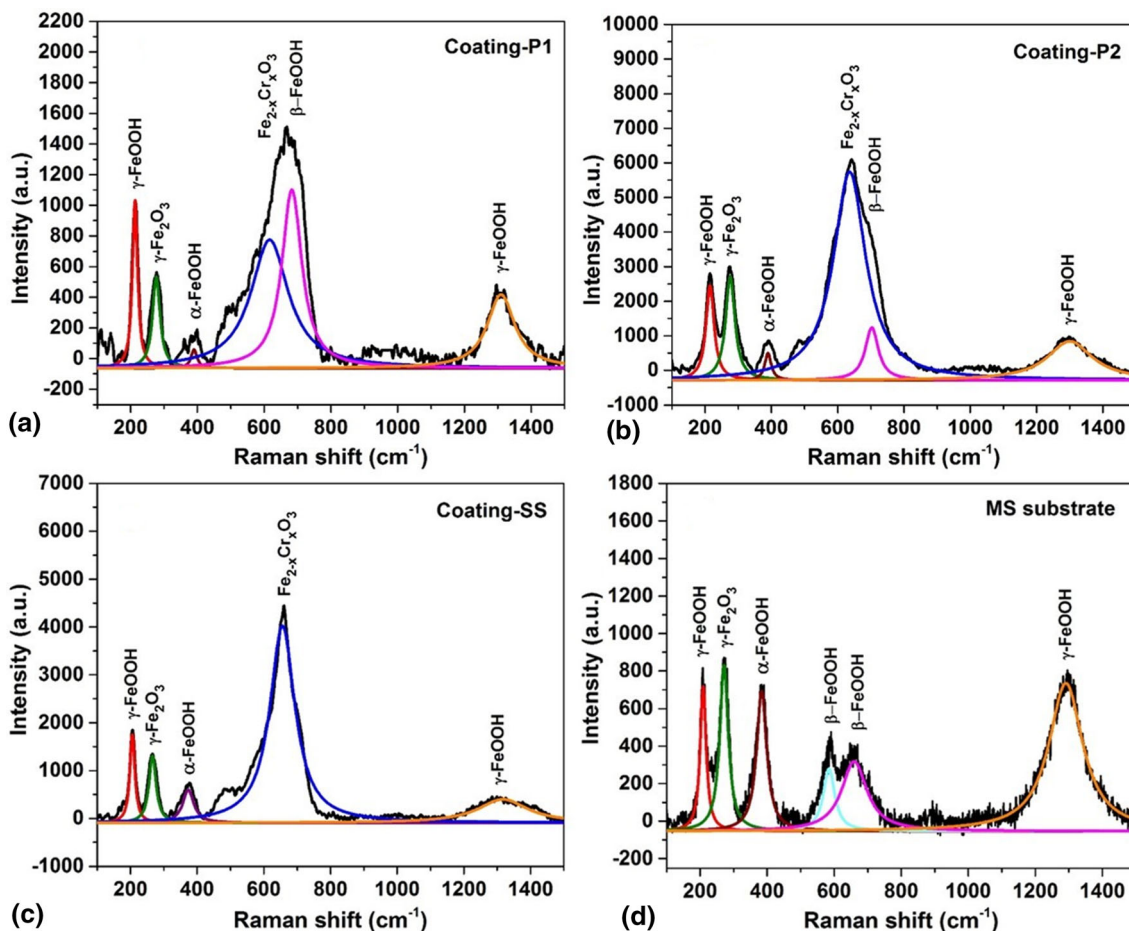
Fig. 11 Raman spectra with deconvolution of peaks of Fe-based rusts formed on the corroded surface of (a, b) P1- and P2-based coatings, (c) stainless steel (SS316L) coating, (d) mild steel
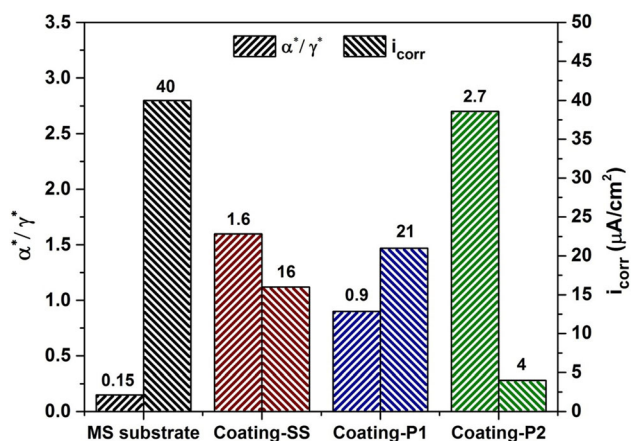

Fig. 12 Bar graph demonstrating the relationship between α^*/γ^* ratio and corrosion current density (i_{corr}) of metallic glass composite coatings, stainless steel (SS316L) coating and mild steel

rust layer. Raman spectra of samples reveal the presence of lepidocrocite (γ-FeOOH), maghemite (γ-Fe$_2$O$_3$), goethite (α-FeOOH), akaganeite (β-FeOOH) and chromium-substituted hematite (Fe$_{2-x}$Cr$_x$O$_3$), except for mild steel

(absence of Fe$_{2-x}$Cr$_x$O$_3$) and Coating-SS (absence of β-FeOOH) (Ref 40-44). Phases like α-FeOOH and Fe$_{2-x}$-Cr$_x$O$_3$ are considered to be protective, whereas γ-FeOOH and β-FeOOH are soluble phases that degrade rapidly in the saline environment.

Nature (stable or unstable) of the rust layer significantly affects the corrosion behavior, therefore, it is important to understand the overall protection ability of corrosion products (Ref 16, 40, 41, 45). In this context, relative protective index (α^*/γ^* ratio) is calculated to establish its relationship with the corrosion current density (i_{corr}) of the samples, and the results are shown in Fig. 12. Parameter α^*/γ^* is the ratio of the total intensity of protective α-FeOOH and Fe$_{2-x}$Cr$_x$O$_3$ phases to the total intensity of unstable γ-FeOOH, γ-Fe$_2$O$_3$ and β-FeOOH phases (Ref 16, 41, 45). Values of α^*/γ^* ratio for Coating-P1, Coating-P2, Coating-SS and mild steel substrate were found to be approximately 0.9, 2.7, 1.6 and 0.15, respectively. From Fig. 12, it can also be that variation in the value of α^*/γ^* ratio is inversely proportional to the values of i_{corr}. The highest value of α^*/γ^* ratio was obtained for Coating-P2

(2.7), i.e., highly stable rusts were formed on the surface of this coating during exposure in NaCl solution, and therefore it exhibited the lowest value of i_{corr} (4 $\mu A/cm^2$). Therefore, it can be said that the best anti-corrosion behavior of Coating-P2 is attributed to the combined effect of dense microstructure, amorphous phase and formation of higher content of protective α-FeOOH and $Fe_{2-x}Cr_xO_3$ phases during corrosion.

Conclusions

In the present work, Fe-based metallic glass composite coatings were synthesized using two different low chromium containing powders $Fe_{73}Cr_2Si_{11}B_{11}C_3$, at. % (P1) and $Fe_{63}Cr_9P_5B_{16}C_7$, at. % (P2) onto mild steel via atmospheric plasma spraying (APS). Microstructural analysis revealed that metallic glass coatings were primarily amorphous in nature (amorphous content > 84%), which resulted because of high glass-forming ability of the compositions and very high cooling rate associated with APS process. Compared to the P1-based coating, the P2-based one exhibited denser microstructure and higher amount of nano-sized intermetallic phases embedded in the amorphous matrix. Because of this, P2-based coating exhibited higher microhardness (1019 $HV_{0.025}$) and lower specific wear rate (6.1 $\pm$ 0.2 x 10^{-6} mm^3/Nm). Besides, corrosion current density of P2-based coating (4 $\mu A/cm^2$) was found to be much lower than that of P1-based one (21 $\mu A/cm^2$), even though it has higher degree of crystallinity. This is attributed to the combined effect of denser microstructure, which was composed of amorphous phase primarily and formation of higher content of protective α-FeOOH and $Fe_{2-x}Cr_xO_3$ phases. Remarkably, P2-based coating showed better wear and corrosion resistance than that of the high Cr-containing stainless steel (SS316L) coating, suggesting its suitability as a protective coating.

References

1. C.A.C. Souza, D.V. Ribeiro, and C.S. Kiminami, Corrosion Resistance of Fe-Cr-Based Amorphous Alloys: An Overview, *J. Non. Cryst. Solids*, 2016, **442**, p 56–66.
2. L. Liu and C. Zhang, Fe-Based Amorphous Coatings: Structures and Properties, *Thin Solid Films*, 2014, **561**, p 70–86.
3. B. Huang, C. Zhang, G. Zhang, and H. Liao, Wear and Corrosion Resistant Performance of Thermal-Sprayed Fe-Based Amorphous Coatings: A Review, *Surf. Coat. Technol.*, 2019, **377**, p 124896.
4. G.Y. Koga, A.M.J. Junior, V. Roche, R.P. Nogueira, R. Schulz, S. Savoie, A.K. Melle, C. Loable, C. Bolfarini, C.S. Kiminami, and W.J. Botta, Production and Corrosion Resistance of Thermally Sprayed Fe-Based Amorphous Coatings from Mechanically Milled Feedstock Powders, *Metall. Mater. Trans. A Phys. Metall. Mater. Sci.*, 2018, **49**(10), p 4860–4870.
5. X.Q. Liu, Y.G. Zheng, X.C. Chang, W.L. Hou, J.Q. Wang, Z. Tang, and A. Burgess, Microstructure and Properties of Fe-Based Amorphous Metallic Coating Produced by High Velocity Axial Plasma Spraying, *J. Alloys Compd.*, 2009, **484**(1–2), p 300–307.
6. Z. Zhou, L. Wang, F.C. Wang, H.F. Zhang, Y.B. Liu, and S.H. Xu, Formation and Corrosion Behavior of Fe-Based Amorphous Metallic Coatings by HVOF Thermal Spraying, *Surf. Coat. Technol.*, 2009, **204**(5), p 563–570.
7. R.Q. Guo, C. Zhang, Y. Yang, Y. Peng, and L. Liu, Corrosion and Wear Resistance of a Fe-Based Amorphous Coating in Underground Environment, *Intermetallics*, 2012, **30**, p 94–99.
8. W. Wang, C. Zhang, Z.W. Zhang, Y.C. Li, M. Yasir, H.T. Wang, and L. Liu, Toughening Fe-Based Amorphous Coatings by Reinforcement of Amorphous Carbon, *Sci. Rep.*, 2017, **7**(1), p 1–10.
9. W. Guo, Y. Wu, J. Zhang, S. Hong, G. Li, G. Ying, J. Guo, and Y. Qin, Fabrication and Characterization of Thermal-Sprayed Fe-Based Amorphous/Nanocrystalline Composite Coatings: An Overview, *J. Therm. Spray Technol.*, 2014, **23**(7), p 1157–1180.
10. A. Concustell, J. Henao, S. Dosta, N. Cinca, I.G. Cano, and J.M. Guilemany, On the Formation of Metallic Glass Coatings by Means of Cold Gas Spray Technology, *J. Alloys Compd.*, 2015, **651**, p 764–772.
11. V. Varadaraajan, R.K. Guduru, and P.S. Mohanty, Synthesis and Microstructural Evolution of Amorphous/Nanocrystalline Steel Coatings by Different Thermal-Spray Processes, *J. Therm. Spray Technol.*, 2013, **22**(4), p 452–462.
12. H. Zhang, Y. Xie, L. Huang, S. Huang, X. Zheng, and G. Chen, Effect of Feedstock Particle Sizes on Wear Resistance of Plasma Sprayed Fe-Based Amorphous Coatings, *Surf. Coat. Technol.*, 2014, **258**, p 495–502.
13. Y. An, G. Hou, J. Chen, X. Zhao, G. Liu, H. Zhou, and J. Chen, Microstructure and Tribological Properties of Iron-Based Metallic Glass Coatings Prepared by Atmospheric Plasma Spraying, *Vacuum*, 2014, **107**, p 132–140.
14. Y.C. Li, C. Zhang, W. Xing, S.F. Guo, and L. Liu, Design of Fe-Based Bulk Metallic Glasses with Improved Wear Resistance, *ACS Appl. Mater. Interfaces*, 2018, **10**(49), p 43144–43155.
15. C. Zhang, L. Liu, K.C. Chan, Q. Chen, and C.Y. Tang, Wear Behavior of HVOF-Sprayed Fe-Based Amorphous Coatings, *Intermetallics*, 2012, **29**, p 80–85.
16. A. Kumar, S.K. Nayak, K. Sarkar, A. Banerjee, K. Mondal, and T. Laha, Investigation of Nano- and Micro-Scale Structural Evolution and Resulting Corrosion Resistance in Plasma Sprayed Fe-Based (Fe-Cr-B-C-P) Amorphous Coatings, *Surf. Coat. Technol.*, 2020, **397**, p 126058.
17. G. Liu, Y. An, Z. Guo, J. Chen, G. Hou, and J. Chen, Structure and Corrosion Behavior of Iron-Based Metallic Glass Coatings Prepared by LPPS, *Appl. Surf. Sci.*, 2012, **258**(14), p 5380–5386.
18. G.Y. Koga, T. Ferreira, Y. Guo, D.D. Coimbrão, A.M. Jorge, C.S. Kiminami, C. Bolfarini, and W.J. Botta, Challenges in Optimizing the Resistance to Corrosion and Wear of Amorphous Fe-Cr-Nb-B Alloy Containing Crystalline Phases, *J. Non. Cryst. Solids*, 2021, **555**, p 120537.
19. R. Moreton and J.K. Lancaster, The Friction and Wear Behaviour of Various Metallic Glasses, *J. Mater. Sci. Lett.*, 1985, **4**(2), p 133–137.
20. A. Kumar, S.K. Nayak, P. Bijalwan, M. Dutta, A. Banerjee, and T. Laha, Optimization of Mechanical and Corrosion Properties of Plasma Sprayed Low-Chromium Containing Fe-Based

Amorphous/Nanocrystalline Composite Coating, *Surf. Coat. Technol.*, 2019, **370**, p 255–268.

21. C. Zhang, K.C. Chan, Y. Wu, and L. Liu, Pitting Initiation in Fe-Based Amorphous Coatings, *Acta Mater.*, 2012, **60**(10), p 4152–4159.

22. W.H. Wang, Roles of Minor Additions in Formation and Properties of Bulk Metallic Glasses, *Prog. Mater. Sci.*, 2007, **52**(4), p 540–596.

23. M. Naka, Effect of Metalloidal Elements on the Microhardness of Iron-Base Glasses, *J. Appl. Phys.*, 1980, **51**(11), p 6006–6009.

24. M. Madinehei, P. Bruna, M.J. Duarte, E. Pineda, J. Klemm, and F.U. Renner, Glass-Formation and Corrosion Properties of Fe-Cr-Mo-C-B Glassy Ribbons with Low Cr Content, *J. Alloys Compd.*, 2014, **615**(S1), p S128–S131.

25. C. Suryanarayana and A. Inoue, Iron-Based Bulk Metallic Glasses, *Int. Mater. Rev.*, 2013, **58**(3), p 131–166.

26. J. Fornell, S. González, E. Rossinyol, S. Suriñach, M.D. Baró, D.V. Louzguine-Luzgin, J.H. Perepezko, J. Sort ,and A. Inoue, Enhanced Mechanical Properties Due to Structural Changes Induced by Devitrification in Fe-Co-B-Si-Nb Bulk Metallic Glass, *Acta Mater.*, 2010, **58**(19), p 6256–6266.

27. H.X. Li, Z.C. Lu, S.L. Wang, Y. Wu, and Z.P. Lu, Fe-Based Bulk Metallic Glasses: Glass Formation, Fabrication, Properties and Applications, *Prog. Mater. Sci.*, 2019, **103**, p 235–318.

28. J. Henao, A. Concustell, I.G. Cano, N. Cinca, S. Dosta, and J.M. Guilemany, Influence of Cold Gas Spray Process Conditions on the Microstructure of Fe-Based Amorphous Coatings, *J. Alloys Compd.*, 2015, **622**, p 995–999.

29. S.K. Nayak, A. Kumar, A. Pathak, A. Banerjee, and T. Laha, Multi-Scale Mechanical Properties of Fe-Based Amorphous/Nanocrystalline Composite Coating Synthesized by HVOF Spraying, *J. Alloys Compd.*, 2020, **825**, p 154120.

30. A. Kumar, R. Kumar, P. Bijalwan, M. Dutta, A. Banerjee, and T. Laha, Fe-Based Amorphous/Nanocrystalline Composite Coating by Plasma Spraying: Effect of Heat Input on Morphology, Phase Evolution and Mechanical Properties, *J. Alloys Compd.*, 2019, **771**, p 827–837.

31. C. Chattopadhyay, K.S.N.S. Idury, J. Bhatt, K. Mondal, and B.S. Murty, Critical Evaluation of Glass Forming Ability Criteria, *Mater. Sci. Technol. (United Kingdom)*, 2016, **32**(4), p 380–400.

32. B.R. Rao, M. Srinivas, A.K. Shah, A.S. Gandhi, and B.S. Murty, A New Thermodynamic Parameter to Predict Glass Forming Ability in Iron Based Multi-Component Systems Containing Zirconium, *Intermetallics*, 2013, **35**, p 73–81.

33. A. Leyland and A. Matthews, On the Significance of the H/E Ratio in Wear Control: A Nanocomposite Coating Approach to Optimised Tribological Behaviour, *Wear*, 2000, **246**(1–2), p 1–11.

34. N.K. Mukhopadhyay, C. Dong, Q. Jianbing, and V.S. Sarma, Nanoindentation Studies on Ti-Zr-Ni Bulk Quasicrystalline Intermetallics, *Philos. Mag.*, 2007, **87**(18–21), p 3109–3115.

35. K. Balani, S.P. Harimkar, A. Keshri, Y. Chen, N.B. Dahotre, and A. Agarwal, Multiscale Wear of Plasma-Sprayed Carbon-Nanotube-Reinforced Aluminum Oxide Nanocomposite Coating, *Acta Mater.*, 2008, **56**(20), 5984–5994.

36. A.A. Burkov and P.G. Chigrin, Effect of Tungsten, Molybdenum, Nickel and Cobalt on the Corrosion and Wear Performance of Fe-Based Metallic Glass Coatings, *Surf. Coat. Technol.*, 2018, **351**, p 68–77.

37. G.S. Ham, K.W. Kim, G.S. Cho, C.P. Kim, and K.A. Lee, Fabrication, Microstructure and Wear Properties of Novel Fe-Mo-Cr-C-B Metallic Glass Coating Layers Manufactured by Various Thermal Spray Processes, *Mater. Des.*, 2020, **195**, p 109043.

38. C. Zhang, Z. Chu, F. Wei, W. Qin, Y. Yang, Y. Dong, D. Huang, and L. Wang, Optimizing Process and the Properties of the Sprayed Fe-Based Metallic Glassy Coating by Plasma Spraying, *Surf. Coat. Technol.*, 2017, **319**, p 1–5.

39. C.P. Jiang, Y.Z. Xing, F.Y. Zhang, and J.M. Hao, Microstructure and Corrosion Resistance of Fe/Mo Composite Amorphous Coatings Prepared by Air Plasma Spraying, *Int. J. Miner. Metall. Mater.*, 2012, **19**(7), p 657–662.

40. S.K. Nayak, A. Kumar, K. Sarkar, A. Pathak, A. Banerjee, and T. Laha, A Study on the Corrosion Inhibition of Fe-Based Amorphous/Nanocrystalline Coating Synthesized by High-Velocity Oxy-Fuel Spraying in an Extreme Environment, *J. Therm. Spray Technol.*, 2019, **28**(7), p 1433–1447.

41. S. Choudhary, A. Garg, and K. Mondal, Relation Between Open Circuit Potential and Polarization Resistance with Rust and Corrosion Monitoring of Mild Steel, *J. Mater. Eng. Perform.*, 2016, **25**(7), p 2969–2976.

42. R. Balasubramaniam, A.V.R. Kumar, and P. Dillmann, Characterization of Rust on Ancient Indian Iron, *Curr. Sci.*, 2003, **85**(11), p 1546–1555.

43. K.F. McCarty and D.R. Boehme, A Raman Study of the Systems $Fe_{3-X}Cr_XO_4$ and $Fe_{2-X}Cr_XO_3$, *J. Solid State Chem.*, 1989, **79**(1), p 19–27.

44. J.E. Maslar, W.S. Hurst, J.J. Bowers, and J.H. Hendricks, In Situ Raman Spectroscopic Investigation of Stainless Steel Hydrothermal Corrosion, *Corrosion*, 2002, **58**(9), p 739–747.

45. P. Bijalwan, C. Singh, A. Kumar, K. Sarkar, N. Rani, T. Laha, A. Banerjee, and K. Mondal, Corrosion behaviour of plasma sprayed Fe based metallic glass ($Fe_{73}Cr_2Si_{11}B_{11}C_3$ (at%) coatings in 3.5% NaCl solution, *J. Non. Cryst. Solids*, 2021, **567**, p 120913.